

Visible Region Polarization Spectroscopic Studies of Template-Synthesized Gold Nanoparticles Oriented in Polyethylene

Nathir A. F. Al-Rawashdeh,[†] Marie L. Sandrock, Carolyn J. Seugling, and Colby A. Foss, Jr.*

Department of Chemistry, Georgetown University, Washington, District of Columbia 20057

Received: September 3, 1997; In Final Form: November 6, 1997

We have obtained visible range polarization spectra of template-synthesized gold nanoparticles oriented in polyethylene (PE). The plasmon resonance extinction bands observed with the incident electric field polarized parallel, perpendicular, and at intermediate angles to the direction of friction orientation are consistent with the long axis of the particles being aligned with the gross orientation axis. For all particle sizes considered (radii 16, 38, and 60 nm) the degree of linear dichroism increases with the amount of gold deposited in the template synthesis step prior to extraction and orientation. The experimental spectra agree with the predictions of the Rayleigh, Maxwell–Garnett, and dynamical Maxwell–Garnett theories only qualitatively. All of these treatments fail to predict the dependence of the spectral extinction intensities on the polarization angle θ . T-matrix scattering calculations suggest that the contribution from electric quadrupole modes cannot be ignored in the 38 and 60 nm radius particles. The calculated θ -dependence of the extinction intensity does not resemble experiment for 16 nm radius particles, but the theory–experiment comparison is more favorable for the larger radius systems. Some possible models for these observations are discussed.

Introduction

The anodic aluminum oxide-based template synthesis method has been applied in numerous studies to prepare micro- and nanoscopic metal particles.^{1–11} The parallel arrays of cylindrical pores in certain anodic aluminas allow for the preparation of uniformly oriented rod- or needlelike metal structures. Furthermore, since the oxide material is transparent over large segments of the visible and infrared spectral regions, the characterization of the optical properties of the metal nanostructures has also been quite straightforward.^{1–3,5,6,8–10}

A few years ago, it was shown that template-synthesized gold particles can be removed from their oxide host and oriented in polymer matrixes.⁸ Recently, we reported the results of a study of the optical spectra of oriented Au particle/polyethylene (PE) composite films, where both the size and the shape of the Au particles were varied.¹⁰ In that study, we found that the gold particle plasmon resonance extinction maxima for incident fields polarized parallel to the direction of particle orientation ($\lambda_{\max}(0)$) were red-shifted relative to the extinction maxima for perpendicular polarization ($\lambda_{\max}(90)$). In general qualitative accord with simple scattering and effective medium theories, the difference between $\lambda_{\max}(0)$ and $\lambda_{\max}(90)$ was found to increase with the particle aspect ratio.

However, we were unable to explain the observed polarization angle dependence of the extinction intensities. Small particle limit treatments such as the Rayleigh scattering¹² and Maxwell–Garnett¹³ theories predict that the extinction intensity for an incident electric field polarized parallel to the long particle axis will be larger than for the perpendicular case.¹⁰ We found this to be qualitatively correct in experiment only for the smallest diameter (32 nm) gold particles. Larger diameter systems exhibited extinction intensity–polarization angle trends opposite

to those predicted by the small particle limit theories. In other words, the extinction in parallel polarization was observed to be lower than in perpendicular polarization.

In this paper, we detail the procedures for preparing oriented Au particle/PE films and the polarization spectra of these composites. We then discuss the observed results in the context of a more rigorous scattering treatment for nonspherical particles developed by Barber and Hill.¹⁴ We also discuss the relative virtues of the so-called dynamical Maxwell–Garnett model⁶ which attempts to incorporate particle size effects into a quasi-static framework and has been used in the past to model experimental data.^{6,9,15}

Theoretical Background

For dilute solutions of particles, the transmittance T of the composite medium can be expressed as^{12,16}

$$T \approx \exp(-NC_{\text{ext}}d) \quad (1)$$

where N is the concentration of particles (m^{-3}), C_{ext} is the extinction cross section (m^2), and d is the optical path length (in m). The extinction cross section is the sum of losses arising from absorption and scattering:

$$C_{\text{ext}} = C_{\text{abs}} + C_{\text{sca}} \quad (2)$$

For particles much smaller than the incident wavelength λ (e.g., radius $a \leq 0.1 \lambda$),¹³ the absorption and scattering cross sections can be related to the particle polarizability α via the expressions^{12,16}

$$C_{\text{abs}} = k \text{Im}\{\alpha\} \quad (3a)$$

$$C_{\text{sca}} = (k^4/6\pi)|\alpha|^2 \quad (3b)$$

where k is the wavevector ($=2\pi/\lambda$), “Im” specifies the imaginary

* Corresponding author.

[†] Current address: Department of Chemistry, Jordan University of Science and Technology, Irbid, Jordan.

part of α , and $|\alpha|^2$ signifies the square modulus of α . The polarizability is a function of the dielectric functions of the particle (ϵ_m) and host medium (ϵ_0) and also the size and shape of the particle. In the small particle (or Rayleigh scattering) limit, the complex polarizability of the particle is given by¹⁷

$$\alpha = \frac{V}{3q} \frac{\epsilon_m - \epsilon_0}{\epsilon_m + \kappa\epsilon_0} \quad (4)$$

where V is the particle volume. The depolarization factor q and screening factor κ are a function of particle shape. The depolarization factor q for a general ellipsoid with semiaxes \mathbf{a} , \mathbf{b} , and \mathbf{c} can be found by solution of Dirichlet's integral,¹⁸ but a very close numerical approximation is the inverse axes ratio¹²

$$q_x \approx \frac{1/x}{1/\mathbf{a} + 1/\mathbf{b} + 1/\mathbf{c}} \quad (5)$$

where x is equal to a , b or c , and q_x is the depolarization factor along the given axis of interest. The screening factor along a given axis is then simply $\kappa_x = (1/q_x - 1)$.¹³

For prolate ellipsoids of revolution, where \mathbf{a} and \mathbf{b} are the semimajor and semiminor axes, respectively, the depolarization factors of relevance are those parallel and perpendicular to the axis of revolution, and are given by

$$q_{\parallel} \approx \frac{1}{1 + 2(\mathbf{a}/\mathbf{b})} \quad (6a)$$

$$q_{\perp} \approx \frac{1}{2 + \mathbf{b}/\mathbf{a}} \quad (6b)$$

For composite systems where the particle density is high and interparticle electromagnetic interactions can occur, it is convenient to define an average complex dielectric constant ϵ , which is a function of the dielectric constants of the particles and their host medium, as well as the volume fraction (f_m) and shape of the particles. Perhaps the most familiar theory is that of Maxwell-Garnett, where ϵ can be found by solution of the equation^{13,19}

$$\frac{\epsilon - \epsilon_0}{\epsilon + \kappa\epsilon_0} = f_m \frac{\epsilon_m - \epsilon_0}{\epsilon_m + \kappa\epsilon_0} \quad (7)$$

The refractive index n and absorption coefficient k are related to the average dielectric constant via $\epsilon = (n + ik)^2$. Equation 7 does not explicitly address particle size, but like the Rayleigh expressions for C_{ext} , the underlying assumption is that the particles are negligibly small relative to the incident wavelength.¹⁹

Since the gold particles examined in our studies are not negligibly small, it is necessary to consider more rigorous scattering theories which apply to particles of any size. For dilute collections of spheres, the Mie theory expression for the extinction cross section is appropriate:^{12,16}

$$C_{\text{ext}} = (2\pi/k^2) \sum_{n=1}^{\infty} (2n+1) \text{Re}\{a_n + b_n\} \quad (8)$$

where a_n and b_n are the scattering coefficients for the electric and magnetic fields, respectively, and the index n indicates the type of induced oscillation ($n = 1$ for dipole, $n = 2$ for quadrupole, etc.). The coefficients a_n and b_n can be calculated in a straightforward manner using Riccati-Bessel functions.^{12,16} For very small particles, the electric dipole term (a_1) predomi-

nates. However, as the particle increases in size relative to λ , the magnetic dipole and higher order electric and magnetic multipole terms become important.

The calculation of extinction cross sections for nonspherical particles is much more difficult. For ellipsoids of revolution or otherwise axisymmetric particles, the treatment for C_{ext} is similar in spirit to that of spheres, namely^{14,20}

$$C_{\text{ext}} = (2\pi/k^2) \sum_{\sigma=1}^2 \sum_{m=0}^{\infty} \sum_{n=m}^{\infty} D_{\sigma mn} \text{Re}\{f_{\sigma mn} + g_{\sigma mn}\} \quad (9)$$

where $f_{\sigma mn}$ and $g_{\sigma mn}$ are the scattering coefficients for the magnetic and electric fields, respectively, and σ , m , and n are the expansion indices of vector spherical harmonic functions.¹⁶ $D_{\sigma mn}$ is a normalization constant.

The calculation of $f_{\sigma mn}$ and $g_{\sigma mn}$ is not trivial and has been done for ellipsoids of revolution by the "separation-of-variables" method^{20,21} and the so-called "T-matrix" method.^{14,22} For our studies, we chose the latter because the source code is commercially available¹⁴ and relatively easy to execute. The details of the T-matrix theory are far beyond the scope of this paper, and the reader is directed to refs 14 and 22. The key point is that this general scattering treatment allows us to consider the size dependence of the electric dipole resonance and the contributions from higher multipoles that Rayleigh-limit treatments do not address.

Mie scattering theory can be used to describe size and shape effects for single particles but does not account for interparticle interactions. On the other hand, effective medium type treatments such as Maxwell-Garnett theory address the effects of interparticle interactions via the volume fraction term f_m but assume that the particles are infinitely small relative to λ . In an attempt to incorporate particle size effects into Maxwell-Garnett theory, we previously adopted an expression for a size-dependent depolarization factor q_{eff} ^{23,24}

$$q_{\text{eff}} = q - \frac{1}{3}k^2b^2 - \frac{1}{9}k^3b^3 \quad (10)$$

where b is either the spherical radius or some characteristic dimension of the particle.⁶ The second term on the right-hand side of eq 10 is the dynamic depolarization factor. The third term accounts for damping associated with the emitted fields of the oscillating particle.^{23,24}

When q_{eff} is incorporated into Rayleigh or Maxwell-Garnett theory (via an effective screening factor $k_{\text{eff}} = 1/q_{\text{eff}} - 1$), an increase in particle size engenders a red shift and damping of the particle plasmon resonance band. While such size effects are seen in experiment, calculated spectra based on eq 10 and Maxwell-Garnett theory tend to overestimate the red shift with increasing particle size.⁶ It should also be emphasized that eq 10 attempts only to address the size dependence of the electric dipole response. Magnetic and higher order electric terms are ignored.

Experimental Section

Porous Anodic Alumina Film Preparation. Prior to anodization, aluminum plates (7 cm \times 7 cm \times 1.00 mm, Aldrich, 99.999%) were electropolished at ca. 0.15 A cm⁻² in a 75–80 °C mixture of sulfuric and phosphoric acid (60:40 v/v mixture of 96% w/v sulfuric acid (Mallinckrodt) and 85% w/v phosphoric acid (Fisher ACS)). The currents were typically applied for 3 min, followed by prompt removal and

rinsing of the Al plates in distilled water. Alumina films containing 38 nm radius pores were prepared by anodizing the polished aluminum plates at 50 V in ca. 17 L of 6% oxalic acid (Mallinckrodt Analytical Reagent). The cathode was a 9 cm × 5 cm × 1 mm lead foil. Voltage was supplied by a Sorensen DCRB-300 dc power source. Within the cell, stainless steel coils connected to an external circulating refrigerator bath (1:1 ethylene glycol/water mix) maintained the anodizing cell temperature between 0 and 3 °C. The cell solution was stirred gently with a helical glass stirrer. Sixty nanometer pore films were prepared in a similar manner, except that the applied voltage was 90 V, and the electrolyte was 2% oxalic acid. Anodization for 12–14 h yielded films of 40–50 μm total thickness. The films were removed from their Al substrate by voltage reduction²⁵ and immersion in 15% phosphoric acid.

Alumina films containing 16 nm radius pores were prepared under the same conditions described above, except that the electrolyte was 4% sulfuric acid, and the applied voltage was 20 V. In this case, the dc voltage was from a Kepco ABC-25-4 dc power supply. Also, the voltage reduction was followed by immersion of the anodized Al plates in 25% sulfuric acid.

The template synthesis of gold particles within the pores of the anodic alumina films has been described in detail elsewhere.^{3–6} Briefly, we used an Anatech Hummer 10 to sputter the barrier side of the porous films with a silver layer ca. 40–50 nm thick. The sputtered films were then clamped between an Al foil-covered glass plate and an O-ring glass joint (2.0 cm diameter) which served as the plating cell base. The Al foil served as the working electrode contact. The reference and counter electrodes were an SSCE²⁶ and platinum gauze strip, respectively. The plating solutions were stirred by gentle bubbling of Ar or nitrogen. Ag and Au were deposited potentiostatically. An EG&G PARC 273 potentiostat was used to supply the voltage and to monitor the amount of charge passed during deposition. A silver foundation was first prepared by depositing 2–4 C from a silver thiocyanate plating solution²⁷ potentiostatically at –0.6 V vs SSCE. The silver plating solution was then removed and the cell rinsed thoroughly. Gold structures were then prepared by potentiostatic deposition of gold from an Au(I) cyanide plating solution (Technic, Inc., Orotemp 24). Once the desired amount of gold was deposited, the silver foundation was removed by placing the composite film in concentrated nitric acid (Mallinckrodt, 92%). The Au/alumina composite films were then rinsed and allowed to dry in air.

To characterize the dimensions of the radius template-synthesized gold particles prepared in the 20 V alumina films, we removed the particles from their host oxide. Small sections of the Au/alumina composites were placed on a track-etched polycarbonate filter membrane (Nuclepore 0.03 μm pores). Dilute aqueous NaOH was introduced to the composite film dropwise while the filter membrane was under suction. When the aluminum oxide material appeared to be dissolved, distilled water was added dropwise to rinse the particles. With the suction off, portions of the liberated particles were transferred to Formvar-coated Cu grids (200 mesh, EM Sciences) by adding to, and then removing from, the filter surface small drops of distilled water. The Cu grids were then allowed to dry at room temperature. Transmission electron microscope (TEM) images were obtained using a JEOL 1200 EX.

The procedure for removing the template-synthesized particles from their oxide host and their orientation in the polyethylene matrix are summarized schematically in Figure 1. A 20 μm

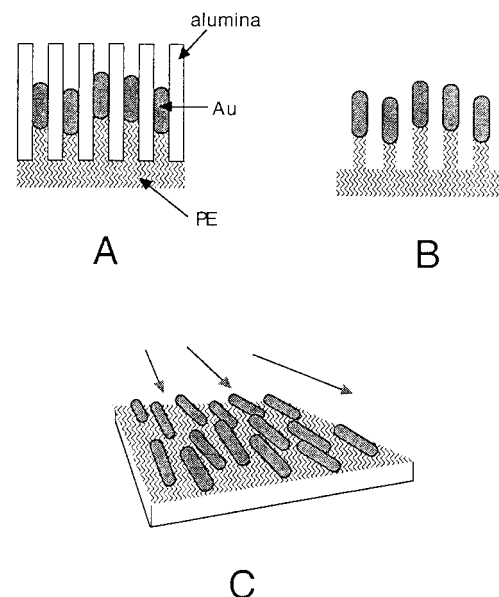


Figure 1. Extraction and orientation of template-synthesized metal particles. (A) Impregnation with polyethylene (PE) under heat and pressure. (B) metal particle/PE composite structure after dissolution of alumina host in aqueous NaOH. (C) Friction orientation of metal and PE nanostructures.

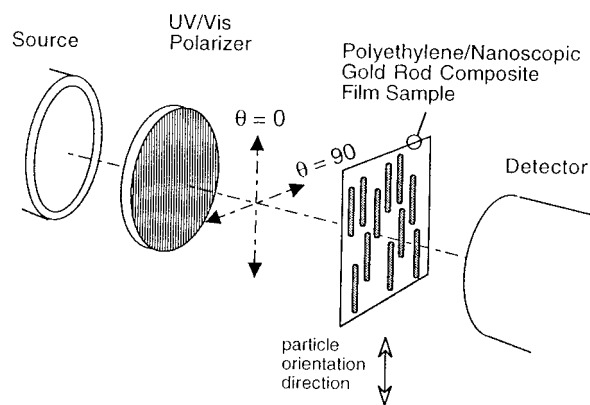


Figure 2. Polarization spectroscopy setup. The polarization angle θ is defined as 0° when the electric field is polarized parallel to the particle orientation direction. $\theta = 90^\circ$ when the electric field is perpendicular to the particle orientation direction.

thick layer of polyethylene (Polysciences) is placed on the barrier side of the Au particle/alumina composite film. (The Au particles are closer to the barrier side.) The two films are then sandwiched between microscope slides and placed on a heating plate. A wood block and ca. 2 kg of weight are placed on the microscope slide/film sandwich. Heat is then applied sufficient to melt the polyethylene and drive it into the pores to contact the Au particles (Figure 1A). After ca. 30 min of heating, the Au/alumina/PE composite is detached from the microscope slides and immersed in 1–2 M aqueous sodium hydroxide. This base solution dissolves the aluminum oxide, leaving fibrils of PE containing the Au particles (Figure 1B). The Au particles are then oriented by brushing the fibrous surface with a soft rubber blade (Figure 1C).

Visible polarization spectra were measured using a Hitachi U-3501 spectrometer equipped with a 210-2130 polarizer accessory. Figure 2 shows a schematic of the optical setup. All spectra were obtained at normal incidence with the polarization angles defined as $\theta = 0^\circ$ when the incident electric field is parallel to the direction of particle orientation and $\theta = 90^\circ$ when the field is perpendicular to the particle main axes.

TABLE 1: Gold Nanoparticle Dimensions from Transmission Electron Microscopic Measurements

host film anodization voltage (V)	gold deposition amount (coulombs) ^a	particle radius ^b (nm)	particle length 2 <i>a</i> (nm)	aspect ratio (<i>a/b</i>)
20	0.20	16 ± 0.5	33 ± 1	1.0
20	0.30	16 ± 0.5	40 ± 5	1.3
20	0.50	16 ± 0.5	67 ± 7	2.2
20	1.20	17 ± 2	220 ± 20	6.3
50	0.30	38 ^b	120 ^d	1.6
50	0.50	38 ^b	200 ^d	2.6
50	0.70	38 ± 2 ^c	256 ^c	3.4
90	0.30	60 ^b	250 ^d	2.1
90	0.50	60 ^b	410 ^d	3.4
90	1.20	60 ^b	980 ^d	8.2

^a Deposited over a 3.14 cm² area. ^b Radius taken from ref 6 TEM measurements on particles grown with different Au loadings, but in porous hosts prepared under identical conditions. ^c Radius or length taken from ref 6 for particles grown under identical conditions for both host film preparation and Au loading. ^d Particle length estimated from least-squares analysis of data in ref 6.

Results

In Table 1 we summarize the measured dimensions of the template-synthesized Au particles as determined by TEM measurements. For the 16 nm radius particles prepared in our lab, the results are based on the observation of particles filtered onto polycarbonate membranes. The data for particles grown in the 50 and 90 V anodic aluminas are taken from ref 6 or from interpolation of plots of aspect ratio versus the number of coulombs deposited.²⁸ From these TEM data, it is clear that we have a systematic relationship between the amount of Au(I) deposited into the porous oxides and the aspect ratio of the resulting Au particles. Unfortunately, we have not been successful in obtaining TEM images of the Au particles within the PE host. Since we are aware that the PE extraction and orientation procedure may cause breakage of the particles, we will refer to Au deposition amounts rather than absolute particle dimensions in the discussion below.

Figure 3 shows a series of polarization spectra of oriented Au particle/PE composites, where the Au particles were prepared in 20 V anodic films. The "0.10 C", "0.30 C", etc., pertain to the amount of Au(I) electrodeposited over the 3.14 cm² working electrode area in the template synthesis step. The numbers on the spectral curves are the polarization angles (θ) as defined in Figure 2. At the lowest level of Au deposition (0.10 C, Figure 3A), the polarization dependence of both λ_{\max} and the extinction intensity is weak. However, as the amount of deposited gold increases, the dependence of both the peak position and intensity on the incident polarization becomes more pronounced (Figure 3B,C). At the largest Au deposition amount (1.0 C, Figure 4) the difference in λ_{\max} between $\theta = 0^\circ$ and $\theta = 90^\circ$ polarizations cannot be determined with certainty because of the working range of the polarizer.²⁹ However, it is clear that the λ_{\max} for $\theta = 0^\circ$ has been shifted into the near-infrared. All of the polarization spectra exhibit an isosbestic point whose wavelength increases with the amount of Au deposited during the particle preparation step.

Similar trends are seen for Au/PE composites prepared from larger radius Au particles. Figure 5 shows the polarization spectra of 38 nm radius Au particles oriented in PE. At low Au loadings (0.3 C, Figure 5A) the polarization effects are weak. At higher deposition amounts, the dependence of λ_{\max} on θ becomes stronger (B and C). Unlike the 16 nm radius systems where the extinction is much greater for parallel polarization, the extinction intensities for the 38 nm radius particles at $\theta =$

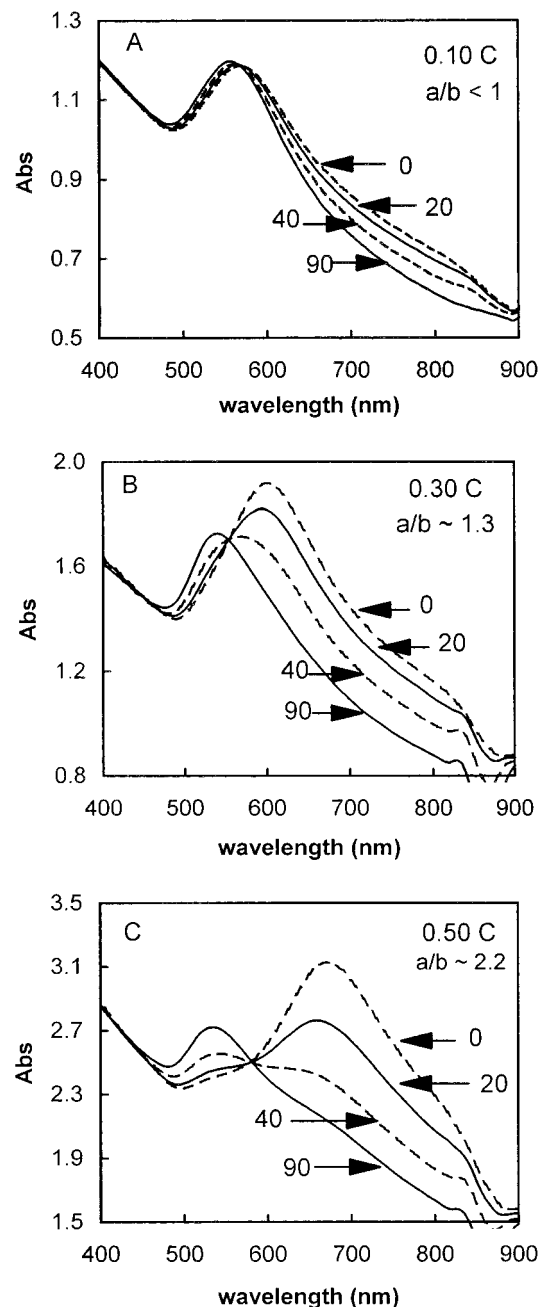


Figure 3. Polarization spectra of 16 nm radius Au particles oriented in PE. The aspect ratios (*a/b*) are estimated from TEM images (see text). Numbers on curves are the polarization angle θ . (A) 0.10 C Au(I). (B) 0.30 C Au(I). (C) 0.50 C Au(I). All spectra are measured against air. Features at ca. 850 nm are detector change artifact.

0° and $\theta = 90^\circ$ are similar. The bands at $\theta = 0^\circ$ are also much broader than in the case of the 16 nm radius Au particle composites.

Finally, Figure 6 shows polarization spectra of 60 nm radius Au particles oriented in PE. For small Au deposition amounts, there is a blue shift and decrease in extinction as the polarization angle changes from 0 to 90 (Figure 6A). However, at larger deposition amounts, the parallel polarization spectra show extinction intensities lower than in the case of perpendicular polarization (Figures 6B,C).

Discussion

For all of the oriented Au particle/PE composite systems considered here, we observe an increase in the degree of

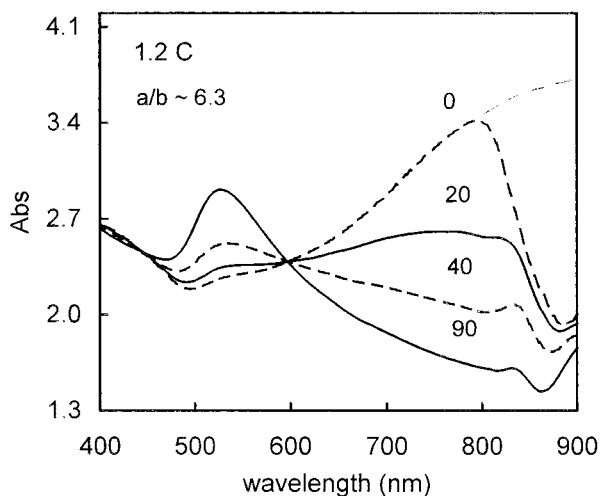


Figure 4. Polarization spectra of 16 nm radius Au particles in PE, at 1.2 C Au(I) loading. Numbers on curves have same meanings as in Figure 3. Aspect ratios (a/b) are estimated from TEM images. Dashed line on $\theta = 0^\circ$ spectrum is probable profile beyond the polarizer working range.

dichroism as the amount of deposited gold in the template synthesis step is increased. This is consistent with an increase in the Au particle aspect ratio. For the smallest radius systems (16 nm), the extinction intensity is higher at $\theta = 0^\circ$ relative to $\theta = 90^\circ$ for all aspect ratios. This intensity dependence on θ is diminished in the 38 nm radius system, where the extinctions at $\theta = 0^\circ$ and 90° are nearly the same. For the largest radius systems (60 nm), the $\theta = 0^\circ$ intensity is greater than the $\theta = 90^\circ$ case only for the smallest Au deposition amounts. For larger deposition amounts and particle aspect ratios, there is an apparent extinction trend reversal.

The dependence of the extinction maximum on polarization angle can be understood qualitatively in terms of eq 4 and the particle dipolar plasmon resonance condition $\text{Re}\{\epsilon_m\} = -\text{Re}\{\kappa\epsilon_0\}$.²⁴ Since the real component of the gold dielectric constant ϵ_m is negative and decreases with wavelength in the visible spectrum, the value of κ determines the wavelength of maximum extinction. When the incident electric field is polarized parallel to the main axis of a rod or prolate ellipsoid, the corresponding screening parameter κ is large and leads to a long wavelength extinction maximum. On the other hand, when the field is perpendicular to the particle axis, κ is small (and approaches unity for infinitely long cylinders), thus leading to an extinction maximum at shorter wavelengths.

The isosbestic point seen in all of the experimental data (except Figure 5A) is highly suggestive of a polarization angle dependence of C_{ext} such as

$$C_{\text{ext}}(\theta) = C_{\text{ext}}(\theta=0) \cos^2 \theta + C_{\text{ext}}(\theta=90) \sin^2 \theta \quad (11)$$

which can be derived from the general expressions for small ellipsoids discussed by Bohren and Huffman.¹⁶ Equation 11 not only predicts an isosbestic point, but predicts that a spectrum of system of nonuniformly oriented particles should show contributions from both long- and short-axis polarization modes even at $\theta = 0^\circ$ and $\theta = 90^\circ$. Figures 3C and 4 show such contributions, demonstrating the limitations of our particle extraction/orientation procedure.

To understand the dependencies of λ_{max} and the total extinction on the polarization angle θ , we calculated extinction spectra using Rayleigh, Maxwell–Garnett, and T-matrix scattering treatments. In all simulations, the gold optical data are

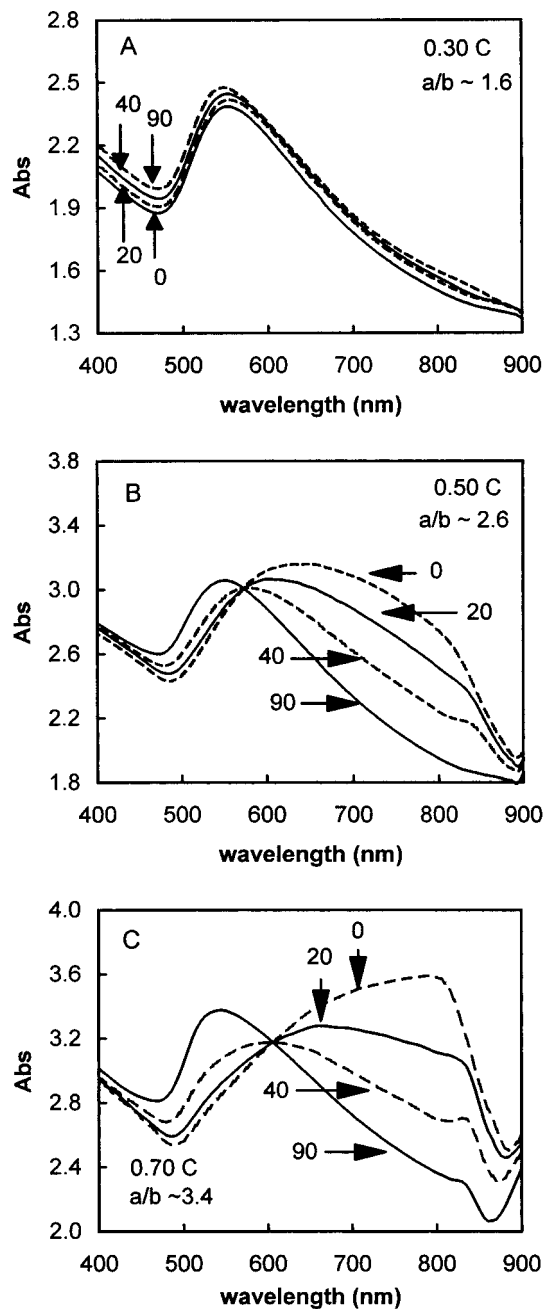


Figure 5. Polarization spectra of 38 nm radius Au particles oriented in PE. Numbers on curves are the polarization angle θ . Aspect ratios (a/b) are estimated from TEM images. (A) 0.30 C Au(I). (B) 0.50 C Au(I). (C) 0.70 C Au(I). All spectra are measured against air. Features at ca. 850 nm are detector change artifact.

taken from Johnson and Christy.³⁰ For the polyethylene host, we assume a refractive index and absorption coefficient of 1.40 and 0, respectively. The experimental refractive index of PE is actually closer to 1.5,³¹ but the process of extraction and orientation probably lead to a less dense host medium for the Au particles.

Comparison with Rayleigh and Maxwell–Garnett Theories. Figures 7 and 8 show polarization spectra calculated using Rayleigh and Maxwell–Garnett theories, both of which inherit eq 4's assumptions regarding particle size ($a, b \ll \lambda$) and polar response (dipole only). In Figure 7, the Rayleigh calculations (plotted as $Q_{\text{ext}} = C_{\text{ext}}/\pi a^2$)³² show that the extinction maximum for incident fields polarized along the particle axis ($\theta = 0^\circ$) occurs at a longer wavelength than the maximum for perpendicular polarization ($\theta = 90^\circ$). The greater the particle aspect

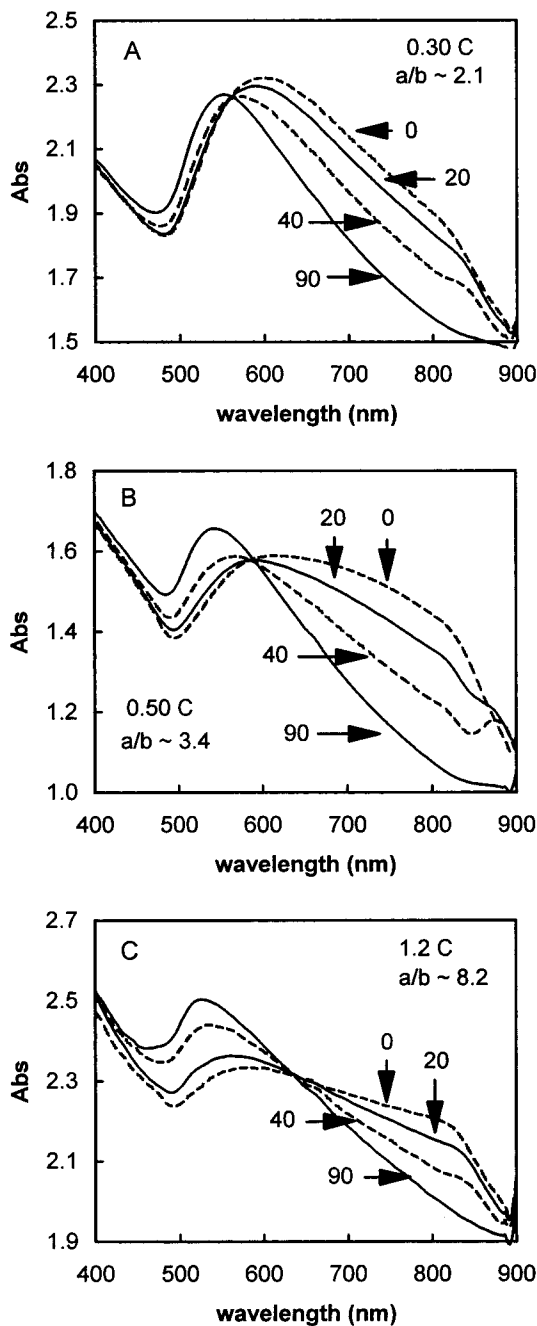


Figure 6. Polarization spectra of 60 nm radius Au particles oriented in PE. Numbers on curves are the polarization angle θ . Aspect ratios (a/b) are estimated from TEM images. (A) 0.30 C Au(I). (B) 0.50 C Au(I). (C) 1.2 C Au(I). All spectra are measured against air. Features at ca. 850 nm are detector change artifact.

ratio, the greater the difference in the spectra at $\theta = 0^\circ$ and $\theta = 90^\circ$. The trends in λ_{\max} with θ and a/b are the same for spectra calculated using Maxwell–Garnett (MG) theory (Figure 8). At a volume fraction $f_m = 0.10$, interparticle interactions do not affect the peak positions greatly. However, the bands are significantly broadened relative to the Rayleigh calculations.

The Rayleigh and MG calculated spectra are similar to experiment only with general regard to the polarization dependence of λ_{\max} . Significantly, the extinction intensity ratios ($A_{\max}(\theta=0^\circ)/A_{\max}(\theta=90^\circ)$ or $Q_{\text{ext,max}}(\theta=0^\circ)/Q_{\text{ext,max}}(\theta=90^\circ)$) are consistently much higher in theory than in experiment. Using either model, we are unable to find an aspect ratio (or combination of a/b and f_m in the MG case) that yields the

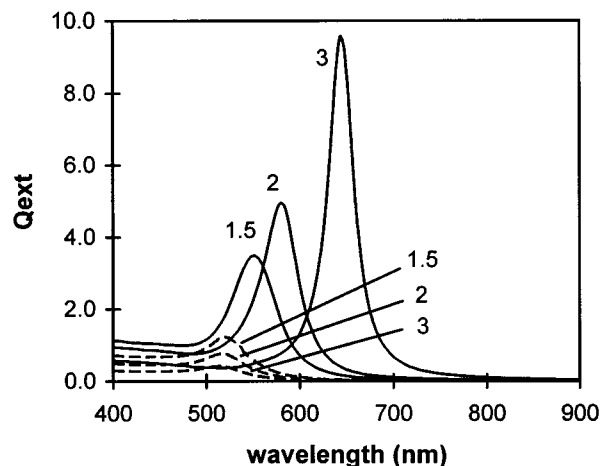


Figure 7. Rayleigh theory calculations (eqs 2–4) for Au ellipsoids with aspect ratios 1.5, 2.0, and 3.0. Solid curves are extinction curves for $\theta = 0^\circ$. Dashed curves correspond to $\theta = 90^\circ$. The host medium is assumed to be nonabsorbing, with $n = 1.4$.

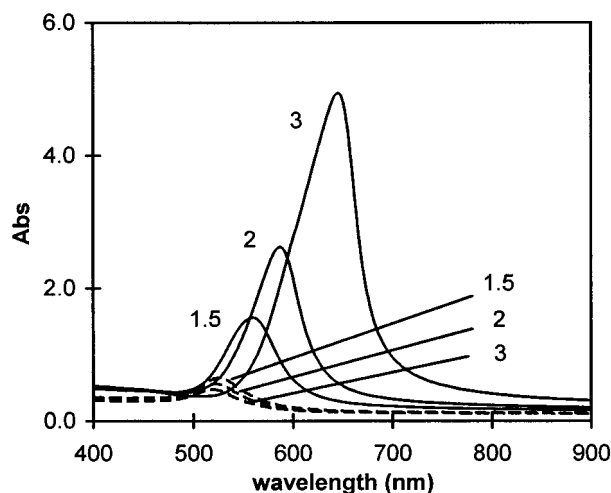


Figure 8. Maxwell–Garnett calculations of extinction spectra for Au ellipsoids with the same aspect ratios as given in Figure 7. The metal volume fraction f_m is equal to 0.10, and the optical path length is 0.10 μm . The solid and dashed curves are spectra for $\theta = 0^\circ$ and 90° , respectively.

experimentally observed combination of large changes in λ_{\max} and moderate changes in extinction with θ .

The first suspect in the consideration of experiment–theory discrepancies is particle size. As discussed in the Theory section, both Rayleigh and MG theories assume that the scattering particle is much smaller than the incident wavelength. Indeed, the radius of the template synthesized gold particles is much smaller than λ in the visible spectrum, but the long axis in many cases is not (see Table 1). As a first step in examining the possible relationships between polarization angle-dependent intensities and particle size, we simulated extinction spectra using a dynamic Maxwell–Garnett model where q_{eff} is given by eq 10. Figure 9 A shows a series of calculated polarization spectra for 16 nm radius Au particles and the same series of aspect ratios considered in Figures 7 and 8. While there is a slight decrease in the ratio $A_{\max}(\theta=0^\circ)/A_{\max}(\theta=90^\circ)$ relative to the simple MG results, the comparison with experiment is still poor.

Since the particle size adjustments according to eq 10 were found to overestimate the red shifts in λ_{\max} as the particle radius is increased,⁶ we also consider another form of q_{eff} , in which the dynamic depolarization factor is omitted and the radiation-

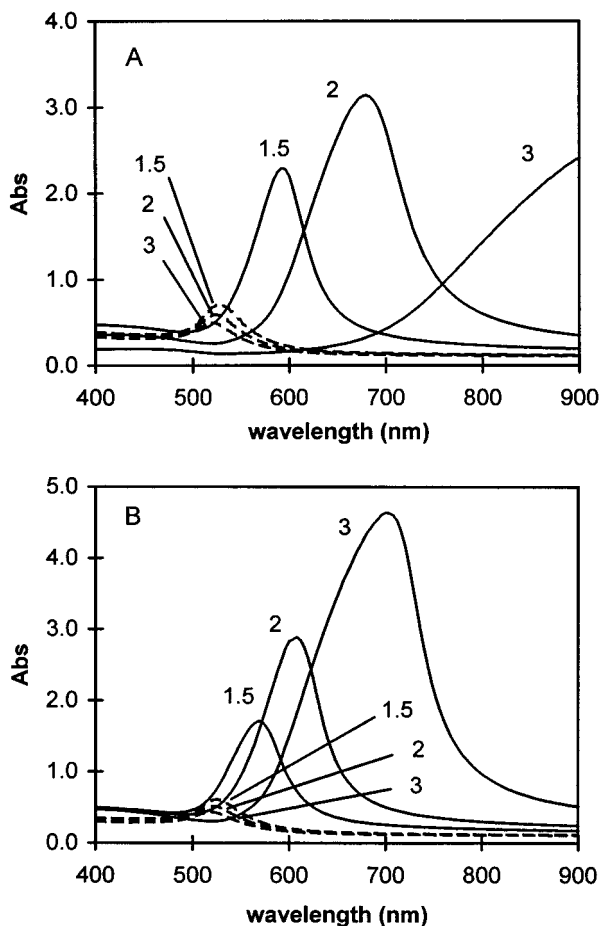


Figure 9. Polarization spectra calculated using dynamic Maxwell–Garnett treatments for 16 nm radius Au ellipsoids with aspect ratios as given in Figures 7 and 8. The metal volume fraction f_m is equal to 0.10, and the optical path length is 0.10 μm . The solid and dashed curves are spectra for $\theta = 0^\circ$ and 90° , respectively. (A) Spectral calculations based on eq 10 definition of q_{eff} , with b = the particle semimajor axis for $\theta = 0^\circ$ and $b = 16$ nm for $\theta = 90^\circ$. (B) Calculations based on radiation damping adjustment only (see text).

damping term is simply related to particle the volume:³³

$$q_{\text{eff}} = q - i(4\pi^2 V/3\lambda^3) \quad (12)$$

As shown in Figure 9B, the omission of the dynamic depolarization term reduces the λ_{max} values for the $\theta = 0^\circ$ polarization spectra of a given particle size and aspect ratio but does not bring the relative intensities in the two polarizations closer to the experimental results.

T-Matrix Scattering Calculation Results. Spectra calculated using the Maxwell–Garnett model modified for particle size effects do not resemble experimental data, even for the smallest particle systems which should be the most amenable to such approximate treatments. Thus, we consider the predictions of the more rigorous T-matrix scattering treatment. As discussed in the Theory section, the full scattering treatment allows us to consider the size dependence of electric dipole modes, as well as contributions of other electric and magnetic polarization modes. We should note that, in our calculation work, we were unable to achieve numerical convergence for aspect ratios greater than about 2.6 for the larger radius systems. However, the calculated spectra for particles that deviate only moderately from the spherical geometry are quite revealing. Also, we note that the T-matrix routines written by Barber and Hill are amenable to both ellipsoids of revolution and finite

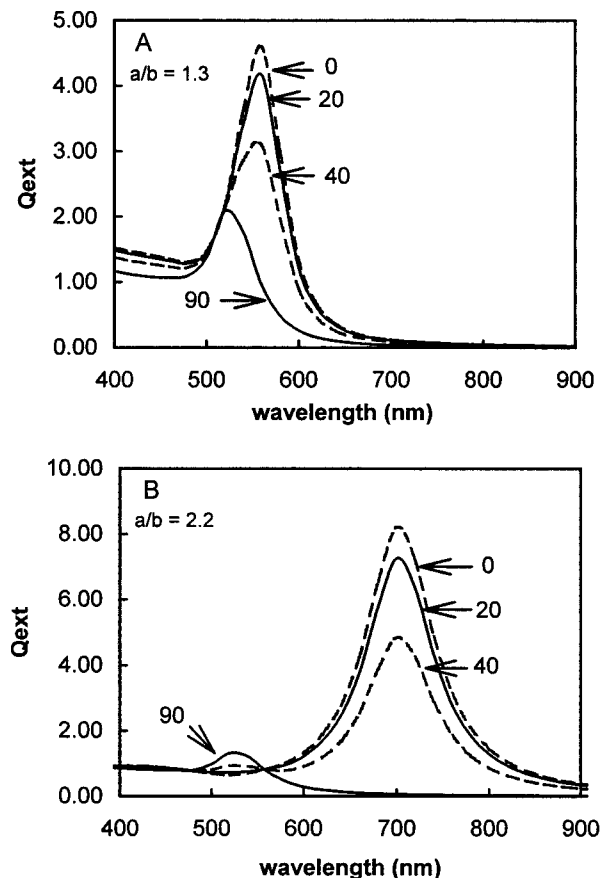


Figure 10. Normalized extinction coefficient spectrum calculated for 16 nm particles using the T-matrix method. Numbers on curves are polarization angles. (A) Aspect ratio = 1.3. (B) Aspect ratio = 2.2. The host medium is assumed to be nonabsorbing, with $n = 1.40$.

cylinders. The experimental particles are neither cylinders nor ellipsoids, but we chose the latter geometry because the computations are somewhat easier. Furthermore, the calculated spectra for the two geometries (holding radius and aspect ratio constant) seem to be very similar, except that the extinction maxima for cylinders is somewhat red-shifted relative to the case of ellipsoids. All T-matrix calculations were performed on a Dell OptiPlex GXMT 5133 personal computer. Calculations of Q_{ext} were done at 20 nm intervals of the visible spectrum, and smoothed curves through these points were generated with Microsoft Excel version 7.0 for Windows.

Figure 10 shows a set of polarization spectra calculated for 16 nm radius gold ellipsoids in a nonabsorbing host medium of refractive index $n = 1.4$. In Figure 10A, the results for an ellipsoid of aspect ratio 1.3 are shown. Compared to Figure 3B, which is a set of spectra for particles whose aspect ratios may be as large as 1.3, the theoretical spectra show a smaller change in λ_{max} between $\theta = 0^\circ$ and $\theta = 90^\circ$ and a larger difference in extinction intensity. However, the change in extinction with θ is much less than predicted by the Rayleigh or simple MG treatments. For an aspect ratio of 2.2, the calculated spectra in Figure 10B are very close to the experimental results (Figure 3C) in terms of λ_{max} . The extinction intensity change with θ is still more severe than seen in experiment.

In Figure 11, the calculated polarization spectra for 38 nm radius Au ellipsoids with aspect ratios 1.3, 1.56, and 2.6 are shown. For the 1.3 and 1.56 aspect ratio systems (Figures 11A,B), the spectra are dominated by particle size and θ -dependent dipolar resonances which are much broader than in the

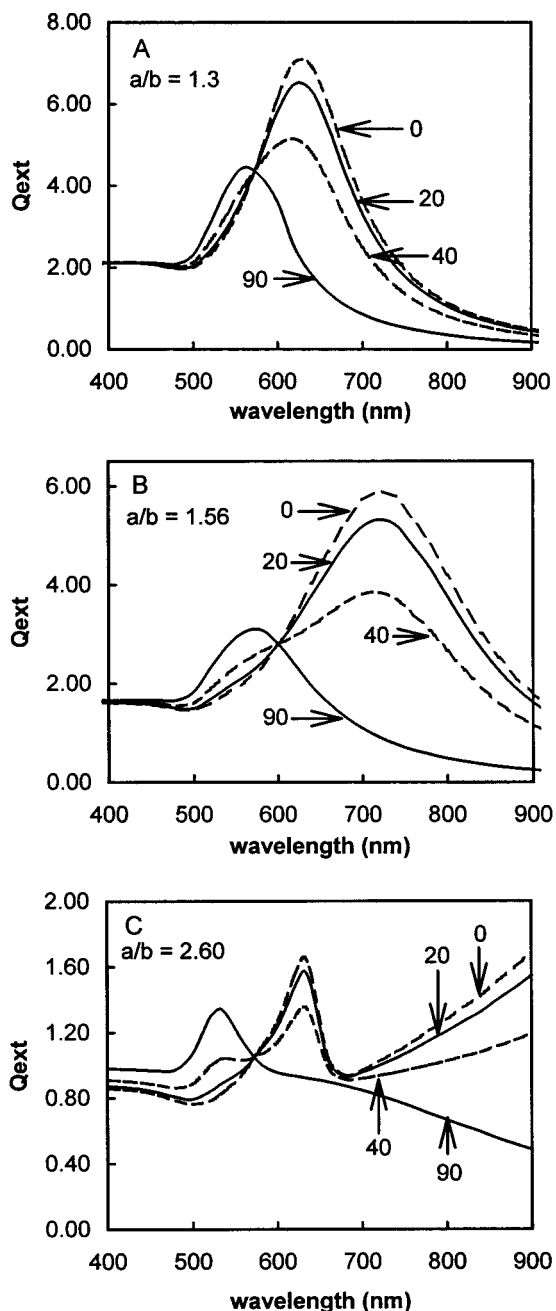


Figure 11. Normalized extinction coefficient spectrum calculated for 38 nm particles using the T-matrix method. Numbers on curves are polarization angles. (A) Aspect ratio = 1.3. (B) Aspect ratio = 1.56. (C) Aspect ratio = 2.60. The host medium is assumed to be nonabsorbing, with $n = 1.40$.

case of the 16 nm radius systems. The extinction intensity differences between the $\theta = 0^\circ$ and $\theta = 90^\circ$ spectra are also considerably diminished, though still greater than seen in experiment. At an aspect ratio of 2.6, the a -axis dipolar resonance is severely red-shifted, and a second (electric quadrupole) resonance appears at ca. 640 nm (Figure 11C).

In comparing the T-matrix results for 38 nm radius Au particles with the experimental data (Figure 5), it would seem that the average aspect ratios of the Au particles in the PE matrix are lower than indicated by the TEM data given in Table 1. For example, the experimental spectra in Figure 5A pertain to particles whose aspect ratios are supposedly ca. 1.6. Yet, the slight change in λ_{max} with θ suggests more spherulike particles. Similarly, the experimental data for oriented Au particles whose aspect ratios are, according to the TEM data, ca. 2.6 (Figure

5B) compare more favorably with the calculated results for $a/b = 1.3$ (Figure 11B). While we were not able to obtain reliable results for an aspect ratio of 3.6, the experimental spectra in Figure 5C may in fact arise from shorter particles (i.e., $a/b = 1.6-2$). These results may be consistent with the template-synthesized Au particles being broken during the extraction and orientation procedure.

Another plausible interpretation of the experimental data for 38 nm radius Au particles in Figures 5B,C is that the long axis resonance component is actually a mixture of electric dipole and quadrupole modes, with a predominance of the latter. In the T-matrix calculation for an aspect ratio of 2.6, the quadrupole resonance maximum occurs at approximately the same wavelength (640 nm) as the λ_{max} at $\theta = 0^\circ$ in the experimental spectrum (Figure 5B). It is also significant that the intensity of the quadrupolar resonance is smaller than a dipole mode in the same wavelength range (i.e., for a particle of identical radius but lower aspect ratio); this may explain the lower extinction intensity seen in the experimental spectra at $\theta = 0^\circ$. A distribution of aspect ratios, originating in the template synthesis step and possibly exacerbated in the extraction/orientation procedure, would then account for the experimental plasmon resonance bands being much broader than the calculated results.

In Figure 12, we show the T-matrix results for Au ellipsoids of radius 60 nm. For particles with $a/b = 1.3$, the $\theta = 0^\circ$ resonance consists of a broad dipole band centered at ca. 760 nm and a quadrupole mode at ca. 550 nm (Figure 12A). The $\theta = 90^\circ$ spectrum shows a very broad dipole mode centered at about 625 nm and a quadrupole mode at ca. 540 nm. As the aspect ratio increases to 1.6 and 2, the quadrupole contribution to the $\theta = 90^\circ$ extinction vanishes, and the dipole mode shifts to shorter wavelengths (540–550 nm). At the same time, the dipole mode in the $\theta = 0^\circ$ maxima red shifts into the near-infrared with increasing aspect ratio, and a weak quadrupole band persists near 600 nm (Figures 12B,C).

At first inspection of the experimental spectra of 60 nm radius particles in Figure 6A, it would seem that the slight change in λ_{max} and extinction intensity with polarization angle is indicative of a particle aspect ratio near unity. However, as can be seen from the calculated spectra in Figure 12A, where the particle aspect ratio is 1.3, we should expect the $\theta = 90^\circ$ maximum to appear as much broader band centered at a longer wavelength (ca. 625 nm) than is seen in experiment (550 nm). To examine this further, we have also calculated the spectra for a 60 nm radius particle of aspect ratio 1.1 and find that the $\theta = 90^\circ$ maximum is ca. 610 nm, a value still well above the experimental λ_{max} . Based on the position of the experimental λ_{max} for the $\theta = 90^\circ$ polarization spectrum shown in Figure 6A, it would appear that the particles are on average distinctly nonspherical. The $\theta = 0^\circ$ experimental spectrum, whose visible region maximum occurs at about 610 nm, may then be due to the quadrupole mode of a more elongated particle.

The experimental spectra for higher gold loadings (Figures 6B,C) compare reasonably well with the calculated spectra in Figure 12B,C. The experimental $\theta = 90^\circ$ maxima occur between 530 and 550 nm. The experimental $\theta = 0^\circ$ spectra show a lower extinction intensity than their $\theta = 90^\circ$ counterparts. For example, in Figure 6C, there is no observed extinction maximum in the visible range for $\theta = 0^\circ$ polarization. Rather, there is simply a sloping plateau between 600 and 850 nm (the upper limit for the polarizer). In the T-matrix results for aspect ratios 1.6 and 2, the $\theta = 90^\circ$ maxima occur at wavelengths near 550 nm, and we see long axis dipole resonances red-shifted into the near-IR, leaving a broad region of lower extinction

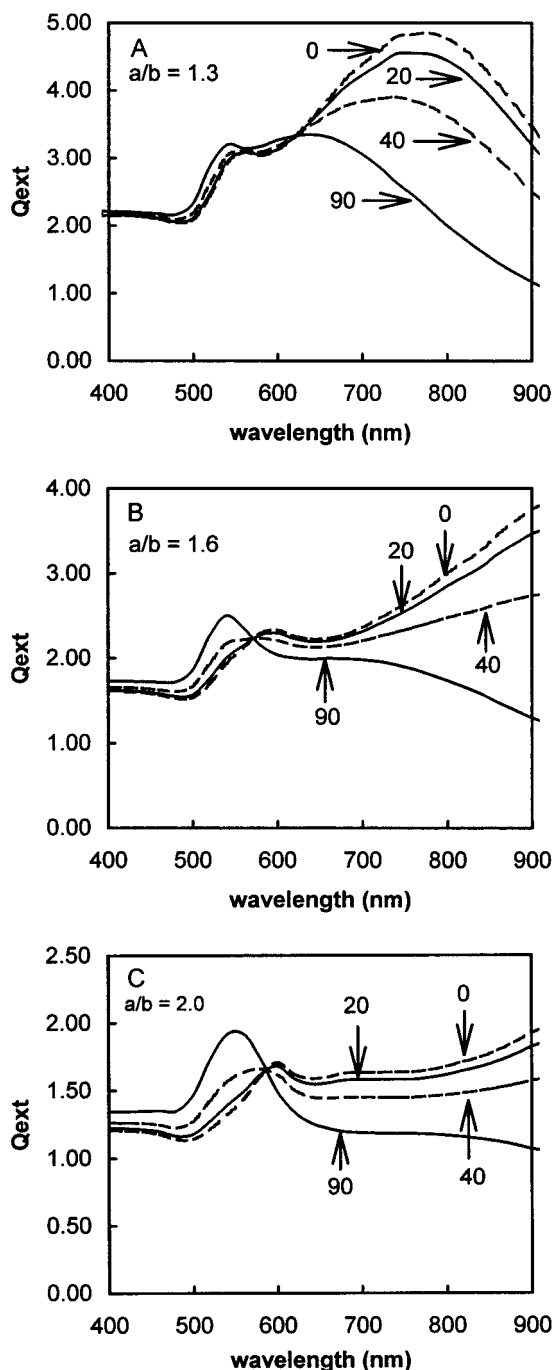


Figure 12. Normalized extinction coefficient spectrum calculated for 16 nm particles using the T-matrix method. Numbers on curves are polarization angles. (A) Aspect ratio = 1.3. (B) Aspect ratio = 1.6. (C) Aspect ratio = 2.0. The host medium is assumed to be nonabsorbing, with $n = 1.40$.

between ca. 600 and 800 nm. While we did not calculate spectra for aspect ratios greater than 2, the contribution from the dipole mode can be expected to diminish in the visible range as the aspect ratio is increased further.

A key trend in the T-matrix calculated spectra is that the difference in extinction intensity between the $\theta = 0^\circ$ and $\theta = 90^\circ$ polarization cases decreases as the particle radius increases. Spectra calculated for 16 nm radius gold ellipsoids do not resemble the experimental results and, indeed, are not very different from spectra simulated using the Rayleigh and Maxwell-Garnett theories. For 38 nm radius particles, the calculated extinction intensities in the $\theta = 0^\circ$ and $\theta = 90^\circ$ polarizations become more similar in magnitude, though the θ

$= 0^\circ$ maxima are still somewhat more intense than the $\theta = 90^\circ$ maxima. For the largest (60 nm) radius particles, even modest aspect ratios of 1.6 and 2 lead to $\theta = 0^\circ$ dipole resonances whose maxima occur well into the near-IR, thus leading to a large region of low extinction in the visible and an overall pattern that is quite like the experimental results.

Scattering Contributions from the Host Medium and Other Effects. The spectral calculations to this point have addressed only the extinction from the particles themselves. Since the scattering calculations do not completely resolve the questions regarding the polarization dependence of the extinction intensities (especially for the 16 nm radius systems), it is useful to consider the contributions from the polyethylene matrix. A thin PE film of uniform thickness does not absorb significantly in the visible spectrum, but the Au particle extraction and orientation procedure certainly imparts roughness to the polymer host which can lead to wavelength-dependent scattering losses. Since the scattering coefficient for a simple dielectric material like polyethylene will increase with decreasing wavelength, we consider the possibility that the theory-experiment discrepancy regarding the θ -dependence of the extinction intensities may be due to background scattering. The extinction intensity of the $\theta = 90^\circ$ bands, which occur at lower wavelengths, would be enhanced by background scattering more than the $\theta = 0^\circ$ bands, which occur at longer wavelengths.

While we know that portions of the PE host film is rendered fibrous by the extraction procedure and that these fibers are oriented during the Au particle orientation step, we do not observe polarization angle-dependent background scattering in the visible region. (The spectra at different θ 's seem to converge in the higher energy region above the plasmon resonance bands.) Thus, we assume that the background scattering is due to spheres whose radii correspond to that of the aluminum oxide pores. The refractive index and absorption coefficient were assumed to be constant at 1.50 and 0, respectively, over the 400–900 nm spectral interval.

Figure 13A shows the $\theta = 0^\circ$ and $\theta = 90^\circ$ spectra for a 16 nm radius Au ellipsoid of aspect ratio 2.2. We assume an Au particle number density of $880 \mu\text{m}^{-3}$ and an Au/PE composite path length of 50 nm. To elevate the $q = 90$ extinction band to an appreciable extent, the PE sphere number density is taken as $10^5 \mu\text{m}^{-3}$ and path length $7.7 \mu\text{m}$. From these calculated spectra, it is clear that background scattering may explain the overall increase in extinction with decreasing wavelength seen in experiment. However, the $\theta = 90^\circ$ resonance band is also quite distorted, and increasing the contribution from background scattering to bring this band closer in intensity to the $\theta = 0^\circ$ resonance only results in washing out the $\theta = 90^\circ$ band completely.

Figure 13B shows a similar calculation for a 38 nm radius Au ellipsoid of aspect ratio 1.56. The Au particle density is assumed to be $93 \mu\text{m}^{-3}$ and the composite path length 100 nm. The PE sphere number density is taken as $2600 \mu\text{m}^{-3}$, with a path length of $0.85 \mu\text{m}$. The addition of background scattering brings the overall appearance of the spectra closer to experiment. However, the relative intensities of the $\theta = 0^\circ$ and $\theta = 90^\circ$ bands cannot be brought into closer agreement with experiment simply by increasing background contributions without severe distortion of the spectra.

In a recent note, we described the preparation and optical properties of dichroic films prepared via friction orientation and pyrolysis of alkanethiol-coated gold particles on Teflon-coated glass slides.³⁴ In that study, we found a similar discrepancy between the θ -dependent extinction seen in experiment and that

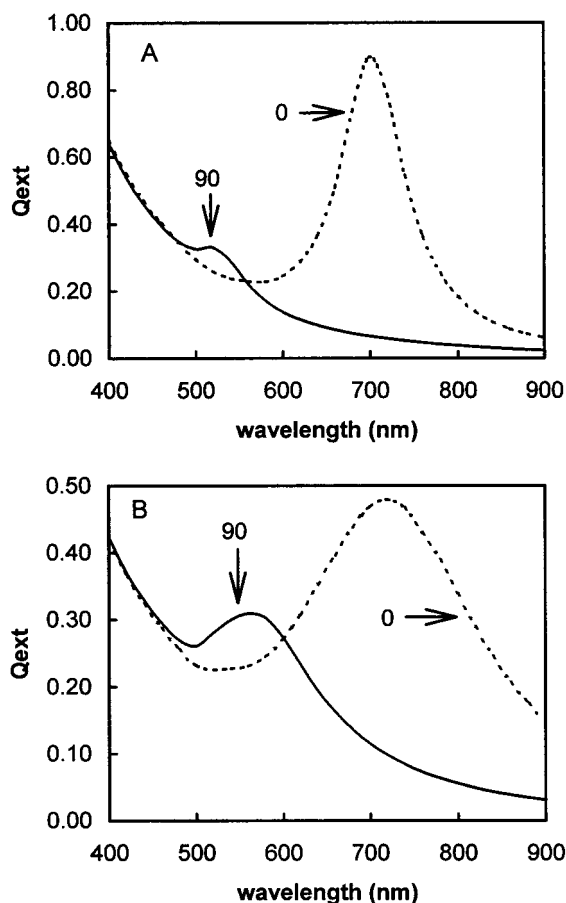


Figure 13. T-matrix scattering calculations for Au ellipsoids with contributions from host medium scattering. Numbers on curves pertain to polarization angle θ . (A) 16 nm radius Au ellipsoids of aspect ratio 2.2, with contributions from 16 nm radius spheres of refractive index $n = 1.50$. (B) 38 nm radius Au ellipsoids of aspect ratio 1.56, with contributions from 38 nm radius spheres of refractive index $n = 1.50$. See text for details.

predicted by effective medium theory when the host medium was assumed to be nonabsorbing. However, when the host medium was modeled as a Lorentz oscillator with a strong resonant mode near the plasmon resonance bands of the gold structures, the θ -dependence of the extinction intensity was subdued, and the simulated spectra better resembled experiment. In that study, the nature of the host medium after flame treatment was unknown, and an absorbing host model seemed appropriate. For the composite films described in this paper, where the host medium is polyethylene, such an interpretation would be difficult to justify.

We also considered the possibility that the gold optical data³⁰ we used in the modeling studies were somehow inappropriate for our nanoscopic structures. For example, the electron mean free lifetime τ decreases with particle size because of surface scattering.²⁴ To examine these effects, we adjusted the free-electron component of the experimental optical data using the procedure discussed by Granqvist and Hunderi³⁵ and then used the adjusted data to model the extinction spectra. Lowering τ damped the extinction intensity of both the $\theta = 0^\circ$ and $\theta = 90^\circ$ bands but did not significantly change their relative intensities.

An intriguing possibility may be inferred from the work of Persson,³⁶ who discusses the damping of plasmon resonance bands by photon-induced electron-transfer (ET) processes between the Fermi level of the metal and unfilled orbitals of the molecules comprising the host medium. Persson's theory

incorporates both ET and particle size effects into an effective mean free lifetime; as the probability of electron transfer increases, the mean free lifetime decreases. As the particle size decreases, the influence the surface ET process on the measured spectrum increases.

The connection between Persson's theory and our experimental results can be seen when one considers the wavelength and particle size dependence of surface electromagnetic enhancement. If ET occurs between the metal particle and the host medium, then it is likely to be subject to local field enhancements. It is well-known that electromagnetic enhancements for gold are large below ca. 2 eV (620 nm) but are diminished above this energy.^{37–39} In the case of our template-synthesized Au particles, surface electromagnetic enhancements would be strongest for $\theta = 0^\circ$ polarization where the plasmon resonance maximum occurs at longer wavelengths. Considering only the polarization of the gold particle (as we did in all of the simulated spectra discussed above), we would always expect the $\theta = 0^\circ$ dipole resonance to show a higher extinction than the $\theta = 90^\circ$ case. However, if the former engenders a stronger surface-enhanced ET, then its extinction will be self-limiting.

While we currently are able to consider its implications in only a qualitative way, the surface-enhanced ET model is quite reasonable when one considers the comparison of experimental and T-matrix spectra for Au particles of different sizes. With regard to the θ -dependence of the extinction intensities, the greatest discrepancy between theory and experiment is seen for the smallest (16 nm radius) particles. Considering the electrodynamic effects discussed by Meier and Wokaun²³ and Zeman and Schatz,²⁴ it is our smallest radius particles that should exhibit the highest surface enhancements. As the particle size increases, radiation damping attenuates electromagnetic enhancements.^{23,24} Consistent with this expectation, as the particle radius increases, the comparison between the experimental polarization spectra and the T-matrix calculations improves; the calculated extinction intensity difference between the $\theta = 0^\circ$ and $\theta = 90^\circ$ dipolar resonances is diminished, and electric quadrupole bands that arise for the higher aspect ratio particles are quite weak. Thus, for the largest particles the θ -dependence of the extinction intensities is accounted for by a rigorous scattering treatment (the T-matrix method). The smaller particles, which produce the higher surface electromagnetic enhancements, may have a more complex relationship with their host medium.

Conclusions

We have prepared dichroic composite materials by removing template-synthesized gold nanoparticles from their alumina hosts and friction-orienting them in polyethylene. The extent of dichroism, as evaluated by the polarization angle dependence of the plasmon resonance maxima (λ_{max}) and extinction intensities, increases systematically with the amount of gold deposited into the porous anodic alumina hosts during the template synthesis step. For particles that are distinctly rodlike (i.e., with aspect ratios greater than unity), the extinction maximum for incident electric fields polarized along the long axis occurs at a longer wavelength than the λ_{max} for polarization along the particle radius.

The observed relationships between λ_{max} , the polarization angle θ , and the particle aspect ratio are in qualitative accord with the predictions of the Rayleigh scattering and Maxwell–Garnett theories. However, the observed dependence of the extinction intensities on θ cannot be explained by these simple treatments which assume that the metal particle is much smaller

than the incident wavelength. Incorporation of particle size effects into Maxwell–Garnett theory does not improve experiment–theory comparisons as they regard extinction intensity– θ relationships.

The spectra obtained using the T-matrix calculation are in poor agreement with the experimental data for the smallest radius particles (16 nm). As the particle radius increases to 38 and 60 nm, the agreement in terms of the θ -dependence of spectral extinction improves. We cannot account for these findings in terms of background scattering from the PE matrix or particle size effects on the metal dielectric properties. However, the unexpectedly low experimental $\theta = 0^\circ$ extinction intensities may result from reductions in the mean free lifetime of electrons in the metal phase arising from metal particle-to-host medium electron transfer.

Acknowledgment. The authors are grateful to the National Science Foundation for its support of this work (Grant DMR 9625151). Acknowledgment is also made to the donors of the Petroleum Research Fund, administered by the American Chemical Society, for partial support of this work. Electron microscopy support was provided by the Lombardi Cancer Center Microscopy and Imaging Shared Resource (U.S. Public Health Service Grant 2P30-CA-51008). N.R. also thanks the Jordan University of Science and Technology (JUST) for financial support during his stay at Georgetown.

References and Notes

- (1) Preston, C. K.; Moskovits, M. *J. Phys. Chem.* **1988**, *92*, 2957.
- (2) Preston, C. K.; Moskovits, M. *J. Phys. Chem.* **1993**, *97*, 8405.
- (3) Tierney, M. J.; Martin, C. R. *J. Phys. Chem.* **1989**, *93*, 2878.
- (4) Foss, C. A., Jr.; Tierney, M. J.; Martin, C. R. *J. Phys. Chem.* **1992**, *96*, 9001.
- (5) Foss, C. A., Jr.; Hornyak, G. L.; Stockert, J. A.; Martin, C. R. *J. Phys. Chem.* **1992**, *96*, 7497.
- (6) Foss, C. A., Jr.; Hornyak, G. L.; Stockert, J. A.; Martin, C. R. *J. Phys. Chem.* **1994**, *98*, 2963.
- (7) Martin, C. R. *Science* **1994**, *266*, 1961.
- (8) Foss, C. A., Jr.; Hornyak, G. L.; Stockert, J. A.; Martin, C. R. *Proc. Mater. Res. Soc.* **1993**, *286*, 431.
- (9) Hornyak, G. L.; Patrissi, C. J.; Martin, C. R. *J. Phys. Chem. B* **1997**, *101*, 1548.
- (10) Al-Rawashdeh, N.; Foss, C. A., Jr. *Nanostructured Mater.* **1997**, *9*, 383.
- (11) Huber, C. A.; Huber, T. E.; Sadoqi, M.; Lubin, J. A.; Manalis, S.; Prater, C. B. *Science* **1994**, *263*, 800.
- (12) van de Hulst, H. C. *Light Scattering by Small Particles*; Dover: New York, 1980.
- (13) Aspnes, D. E. *Thin Solid Films* **1982**, *89*, 249.
- (14) Barber, P. W.; Hill, S. C. *Light Scattering by Particles: Computational Methods*; World Scientific: River Edge, NJ, 1990.
- (15) Hornyak, G. L.; Patrissi, C. J.; Martin, C. R.; Valmalette, J.-C.; Dutta, J.; Hofman, H. *Nanostruct. Mater.* **1997**, *9*, 575.
- (16) Bohren, C. F.; Huffman, D. R. *Absorption and Scattering of Light by Small Particles*; Wiley: New York, 1983.
- (17) Equation 4 can be derived from the expression in ref 11 (p 70), where L_j is the same as q_x in this paper, and $\kappa = 1/q - 1$.
- (18) (a) Fricke, H. *J. Appl. Phys.* **1953**, *24*, 644. (b) Stoner, E. C. *Philos. Mag.* **1945**, *36*, 803.
- (19) Maxwell-Garnett, J. C. *Philos. Trans. R. Soc. London* **1904**, *302*, 385.
- (20) Asano, S. *Appl. Opt.* **1979**, *18*, 712.
- (21) Asano, S.; Yamamoto, G. *Appl. Opt.* **1975**, *14*, 29.
- (22) Varadan, V. K.; Varadan, V. V. *Acoustic, Electromagnetic and Elastic Wave Scattering: Focus on the T-Matrix Approach*; Pergamon: New York, 1980.
- (23) Meier, M.; Wokaun, A. *Opt. Lett.* **1983**, *8*, 851.
- (24) Zeman, E. J.; Schatz, G. C. In *Proceedings of the 17th Jerusalem Symposium*; Pullman, B., Jortner, J., Nitzan, A., Gerber, B., Eds.; Reidel: Dordrecht, Holland, 1984; p 413.
- (25) Furneaux, R. C.; Rigby, W. R.; Davidson, A. P. U.S. Patent No. 4,687,551, Aug 18, 1987.
- (26) The silver–silver chloride reference electrode (SSCE) consisted of an AgCl-coated silver wire immersed in 4 M KCl saturated with AgCl. The reference solution was separated from the plating solution phase by a porous glass junction (Vycor).
- (27) Shumilova, N. A.; Zutaeva, E. V. In *Encyclopedia of Electrochemistry of the Elements*; Bard, A. J., Ed.; Marcel-Dekker: New York, 1978; Vol. 8.
- (28) The aspect ratios for the 38 and 60 nm radius particles were estimated from one-parameter least-squares analysis of the a/b (versus number of coulombs) data in ref 6 (the deposition area is the same for the two studies). For the 38 nm radius system, $a/b = (5.2 \pm 0.2) \times \#C$. For the 60 nm radius system, $a/b = (6.8 \pm 0.5) \times \#C$.
- (29) The spectrum of two crossed polaroids shows zero transmittance between 330 and 700 nm, less than 0.02% T between 700 and 782 nm, and less than 0.05% between 782 and 790 nm. We do not consider the data above 790 nm quantitatively meaningful.
- (30) Johnson, P. B.; Christy, R. W. *Phys. Rev. B* **1972**, *6*, 4370.
- (31) See for example: Ashok, J.; Varaprasad, P. L. H.; Birch, J. R. In *Handbook of Optical Constants of Solids II*; Palik, E., Ed.; Academic Press: New York, 1991.
- (32) For spheres, the quantity \hat{a} is simply the sphere radius. For ellipsoids of revolution with semimajor axis \mathbf{a} and semiminor axis \mathbf{b} , \hat{a} is taken as equal to $\mathbf{a}(\mathbf{a}/\mathbf{b})^{2/3}$. See ref 14, p 103.
- (33) Wokaun, A.; Gordon, J. P.; Liao, P. F. *Phys. Rev. Lett.* **1982**, *48*, 957.
- (34) Lu, A. H.; Lu, G. H.; Kessinger, A. M.; Foss, C. A., Jr. *J. Phys. Chem.*, accepted.
- (35) Granqvist, C. G.; Hunderi, O. *Phys. Rev. B* **1977**, *16*, 122.
- (36) Persson, B. N. J. *Surf. Sci.* **1993**, *281*, 153.
- (37) Schatz, G. C. In *Surface Enhanced Raman Scattering*; Chang, R. K., Furtak, T. E., Eds.; Plenum Press: New York, 1982.
- (38) Allen, C. S.; Schatz, G. C.; van Dyne, R. P. *Chem. Phys. Lett.* **1980**, *75*, 201.
- (39) Chase, B.; Parkinson, B. *J. Phys. Chem.* **1991**, *95*, 7810.